Characterization of budding twigs of flower-type zinc oxide nanocrystals for the fabrication and study of nano-ZnO/p-Si heterojunction UV light photodiode

Amit Kumar Bhunia[1],* and Satyajit Saha[2]

[1] Department of Physics, Government General Degree College at Gopiballavpur-II, Beliaberah, Jhargram, West Bengal 721517, India
[2] Department of Physics, Vidyasagar University, Paschim Medinipur, Midnapore, West Bengal 721102, India

ABSTRACT

In this work, we focused on the study of the structural and optical properties of chemical precipitation-derived special shape (budding twigs of flower-type) ZnO nanostructures for optoelectronic and photodetection applications. The structural and optical properties of the budding twigs of Jasminum flower-like ZnO nanocrystals have been studied and discussed in detail from the XRD, HRTEM, UV–Vis, and photoluminescence spectra. The grown ZnO nanocrystals have been coated on the p-Si substrate to fabricate nano-ZnO/p-Si heterojunction photodiode. The junction properties of the fabricated photodiode were examined by measuring ultraviolet (UV)-light-dependant ($\lambda \sim 366$ nm) and dark condition current (I)–voltage (V) as well as capacitance (C)–voltage (V) characteristics. The photodetection properties of the diode in the UV light region have been examined. The diode has well-defined rectifying behavior with a photoresponsivity and external photodetection efficiency of 0.065 and 21.5%, respectively. The observed barrier height and donor concentration under dark condition were ≈ 0.25 eV and 2×10^{17} cm^{-3}, respectively. The change in heterojunction capacitance, barrier height, the depletion width, and other parameters of the heterojunction photodiode under UV illumination has been discussed. The qualities of the device demonstrate that it tends to be used for UV photodetection applications in nano-optoelectronic and photonic devices.

1 Introduction

Zinc oxide (ZnO) is an optically transparent (> 80%) II–IV direct band gap semiconductor material with large exciton binding energy (60 meV) and huge band gap energy (3.37 eV at room temperature) [1, 2]. In the nanoscale, ZnO showed extraordinary optical, structural, and optoelectronic properties [3, 4]. Nanostructured ZnO-based devices have drawn critical consideration of the specialists over the previous decade for their conceivable arrangement in an

Address correspondence to E-mail: amitphysics87@gmail.com

assortment of electronic and optoelectronic applications. ZnO nanostructure-based devices have found widespread applications in solar cells, different optoelectronic applications, gas sensors, biosensors, Schottky diodes, memory devices, heterojunction diodes, and UV-light-based photodetectors and other various devices [5–11, 53]. ZnO-based ultraviolet photodetectors have potential focal points that incorporate its strong UV response, plausibility of basic and low-cost processing, and chemical stability even in an unfavorable environment [12, 13, 52, 53, 58]. Researchers have allegedly used various techniques for growing various shapes and size ZnO nanostructures [14–16]. ZnO nanostructure with different size and shape along with their structural and optical properties are important in the recent research field due to their optical and optoelectronic applications [17–20]. The fabrication of homo- and heterojunction photodiodes based on semiconductor nanomaterials and different 2D materials is a developing field that considers practical use of nanotechnology in electronics [21–28]. The expense and performance of such devices are the most challenging tasks in the research community. Different procedures have been widely used to fabricate high-performance, homo and heterojunctions based on ZnO semiconductors because of its phenomenal electrical and optical properties [29–31, 37]. Few research works have been exhibited for heterojunctions dependent on ZnO nanostructure with Si utilizing various techniques [32–34, 37]. Sometimes the results are unsatisfactory overall and prerequisite for significant expense. Various physical techniques used in different cases can surely bring about superior diodes; however, the manufacture costs are very high, restricting their industrial applications [34–36]. Consequently, there is a requirement for alternative, cost-effective methods to fabricate homo and heterojunction diodes based on different size, shape ZnO semiconductor nanocrystals. Dutta et al. reported the low-cost sol–gel fabrication of bulk ZnO-based heterojunction [37]. Kabra et al. and Sing et al. reported low-cost fabrication and electrical characterization of ZnO nanostructure-based heterojunction diode [31, 38].
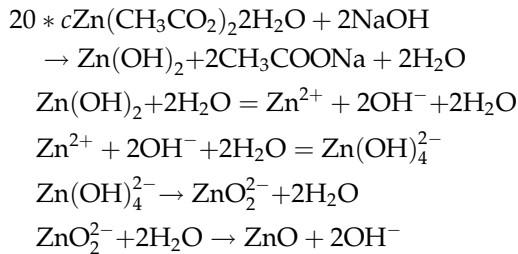
In this research, an attempt is made on the fabrication of heterojunction based on low-cost special shape ZnO nanostructure on p-Si. This work makes a systematic investigation of the itemized structural, surface morphological examination involving grain size, lattice parameters, defect density, strain parameters, and optical investigation of chemical precipitation-derived budding twigs of flower-type ZnO nanostructures in regard of optical bandgap, refractive index, optical dielectric constant, and other various optical parameters including photoluminescence properties. This research reports a technique for the fabrication of low-cost, UV-light-dependent heterojunction diode based on budding twigs of flower-type ZnO nanocrystals on p-type Si (p-Si). The current (I)–voltage (V) and capacitance (C)–voltage (V) characteristics of the fabricated heterojunction were studied under dark and UV illumination. The different electrical parameters and UV photodetection properties of proposed nano-ZnO/p-Si heterojunction diode have been estimated and the results are discussed.

2 Experimental

2.1 Grown of ZnO nanocrystals

The ZnO nanocrystals were fabricated by a simple chemical precipitation technique. In this process, we used zinc acetate and sodium hydroxide. First 0.25 mole zinc acetate solution was prepared by dissolving zinc acetate within the water. Sodium hydroxide (NaOH) solution of 0.2 M was prepared by dissolving NaOH in water. So prepared 50 ml 0.25 M zinc nitrate solution was stirred magnetically for 20 min, then 50 ml 0.2 M NaOH solution was added drop wise for 30 min. After the addition of a few drops NaOH solution with the zinc nitrate solution, a white color appears within the mixed solution. After the addition of total NaOH solution, a white precipitation formed within the mixed solution. The complete mixture solution was kept under constant magnetic stirring for 20 h. The final product is collected by the centrifugation six times with washed fresh water. The collected sample is annealed under 200 °C for 2 h. The so-prepared sample is ready for different characterizations and device fabrication. The following reaction occurs in this chemical precipitation growth process:

$20 * c\text{Zn}(\text{CH}_3\text{CO}_2)_2 2\text{H}_2\text{O} + 2\text{NaOH}$
$\rightarrow \text{Zn(OH)}_2 + 2\text{CH}_3\text{COONa} + 2\text{H}_2\text{O}$

$\text{Zn(OH)}_2 + 2\text{H}_2\text{O} = \text{Zn}^{2+} + 2\text{OH}^- + 2\text{H}_2\text{O}$

$\text{Zn}^{2+} + 2\text{OH}^- + 2\text{H}_2\text{O} = \text{Zn(OH)}_4^{2-}$

$\text{Zn(OH)}_4^{2-} \rightarrow \text{ZnO}_2^{2-} + 2\text{H}_2\text{O}$

$\text{ZnO}_2^{2-} + 2\text{H}_2\text{O} \rightarrow \text{ZnO} + 2\text{OH}^-$

At first, Zn^{2+} ions reacted with OH^- ions and formed $[\text{Zn (OH)}_4]^{2-}$ ($\text{Zn}^{2+} + 2 \text{OH}^- + 2 \text{H}_2\text{O} \rightarrow \text{Zn(OH)}_4^{2-}$). At that point, after small reaction time, later under magnetic stirring saturation, ZnO nuclei can form $[\text{Zn(OH)}_4^{2-} \rightarrow \text{ZnO}_2^{2-} + 2\text{H}_2\text{O} \rightarrow \text{ZnO} + 2\text{OH}^-]$. These ZnO cores by then grow more to make the round ZnO particles. ZnO nuclei are aggregated and shaped further to the structure of the ZnO nanocrystal.

2.2 Device fabrication

The ZnO thin film was formed on the p-type Si substrate with (100) orientation using a spin coating technique. The measured resistivity of used p-type Si substrate is of the order of 5 Ω cm. Before the thin film preparation, the Si substrate is cleaned by standard process followed by etching in 1% dilute hydrofluoric acid. The film was then annealed at 100 °C for 45 min. Aluminum (Al) contacts were then formed over the p-Si substrate and the ZnO film by vacuum evaporation as indicated in Fig. 12b. Aluminum was used to eradicate any possibility of rectification through the contacts, as its work function (4.08 eV) is higher than that of ZnO (< 4 eV). The Al contacts are assumed to form ohmic contacts. The schematic structure of nano-ZnO/p-Si heterojunction photodiode is shown in Fig. 12b.

2.3 Characterization methods and instrumentations

The current (I)–voltage (V) characteristics, capacitor (C)–voltage (V) characteristics of the as-prepared nano-ZnO/p-Si heterojunction in dark, and air mass 1.5 illuminations (XES-151S) with a power density with 100 mW/cm² have been measured. Agilent B1500A semiconductor device analyzer has been used to perform the measurement of I–V and C–V characteristics of the fabricated heterojunction device in the condition of dark and UV light irradiation with wavelength (λ) ≈ 366 nm.

The characterization details for UV–Vis spectroscopy, emission spectroscopy, XRD, and HRTEM study have been discussed in the supplementary document (see Supplementary S1).

3 Results and discussion

3.1 UV–Vis spectrum

The absorption spectrum of the ZnO NCs is shown in Fig. 1a which shows the absorbance maxima at the wavelength (λ) ≈ 360 nm. The bandgap of the sample is determined from the Tauc's formula [38]: $(\alpha h\upsilon)^2 = c(h\upsilon - E_g)$. The plot of $(\alpha h\upsilon)^2$ vs. $(h\upsilon)$ of the sample is shown in Fig. 1b. The calculated band gap energy is 3.72 eV. The absorbance maxima at λ ≈ 360 nm (< 400 nm) is because of the electron transitions (O_{2p}–Zn_{3d}) within the intrinsic band gap absorption. This shifting and band gap changes happen because of nanoscale confinement that affected the size and microstructure changes within the nanoregion. The Urbach energy (E_U) is likewise studied from the accompanying relation (1) [40]:

$$\alpha = \alpha_0 \exp\left[\frac{h\gamma}{E_u}\right] \tag{1}$$

where $h\upsilon$ = photon energy. The plot of $\ln(\alpha)$ vs. $h\upsilon$ is shown in Fig. 1c. The average Urbach energy (E_U) value is 1.969 eV. This result determined that the estimation of the E_U is greater than other reported values [41, 42]. This adjustment in the E_U might be the cause of the nanoscale confinement effect. Distinct optical parameters are tabulated in Table 1 (see Table 1). The refractive index (n) of the semiconductor ZnO NCs in terms of reflectance (R) and extinction coefficient (K) can be expressed by the following equation (2) [43]:

$$n = \left(\frac{1 + R}{1 - R}\right) + \sqrt{\left\{\frac{4R}{(1 - R)^2}\right\} - K^2} \tag{2}$$

where $K = \alpha\lambda/4\pi t$ and $R = 1 - (A + T)$, A = absorption, T = transmittance, λ is the wavelength, and t is the sample thickness. The graphical variations of the K and refractive index (RI) as a function of λ are shown in Fig. 1e and f, respectively. The RI of ZnO NCs increases up to λ ≈ 372 nm with maximum RI
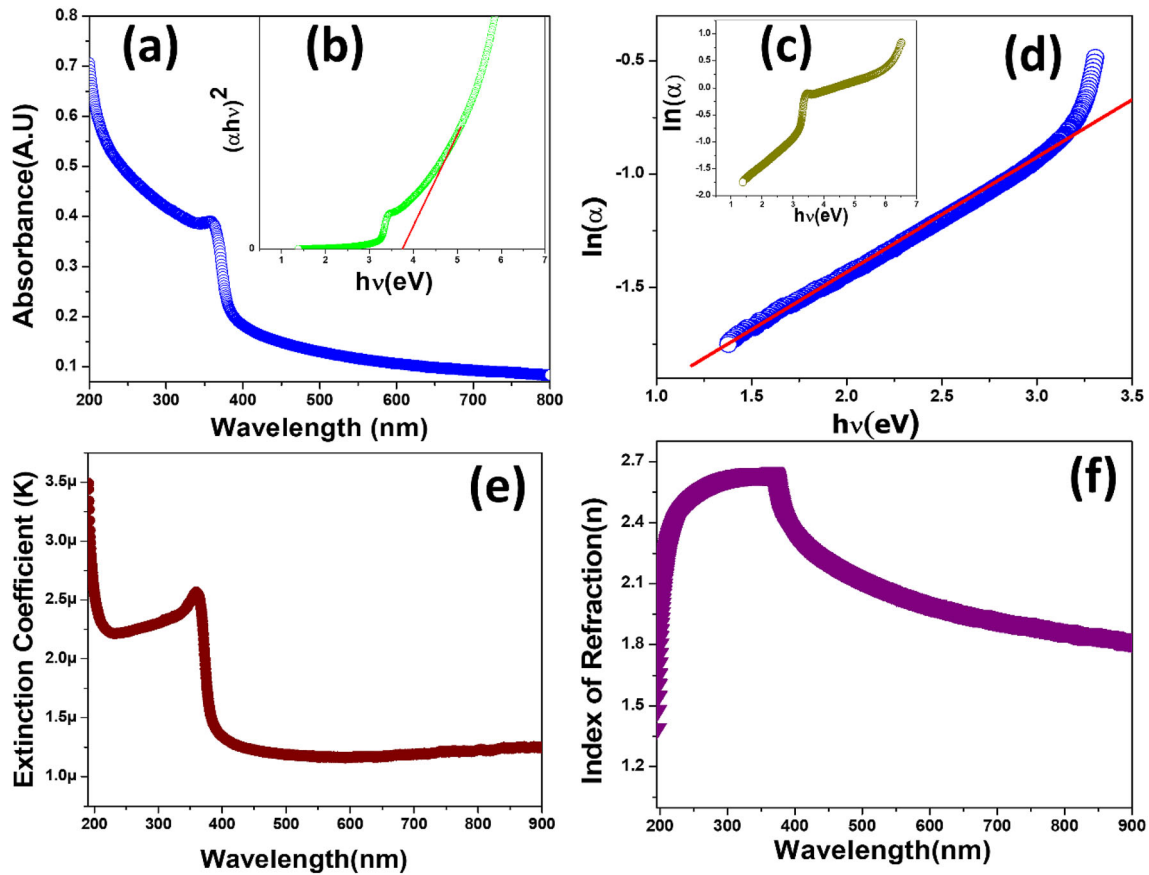
Fig. 1 a Absorption spectroscopy of ZnO NCs; **b** bandgap determination plot or Tauc's plot; **c** plot of ln α vs. photon energy (hυ) with full energy scale of the ZnO NCs; **d** plot of ln α vs. hυ with lower energy scale and corresponding straight line fitting; **e** variation of extinction coefficient (K) vs. wavelength (λ); **f** variation of refractive index (n) vs. wavelength (λ) of ZnO NCs

Table 1 Different optical parameters of ZnO NCs measured from UV–Vis and photoluminescence spectrum

| Sample	Absorption spectrum			Emission spectrum	
	Absorption peak maximum wavelength (nm)	Band gap energy (eV)	Urbach energy (eV)	Peak in nm (area)	Peak in nm (area)
ZnO NCs	360	3.72	1.969 eV	385.531 ± 0.279 (6.503 ± 0.093)	574.128 ± 0.205 (36.279 ± 0.105)

2.66, beyond this wavelength RI gradually decreases up to $λ ≈ 900$ nm. The rate of growth of RI with respect to wavelength is faster than the rate of decay. Beyond $λ ≈ 560$ nm the rate of decay is comparatively slow (toward constant value). The optical conductivity ($σ$) with unit (s^{-1}) can be determined by the following equation (3) [44]:

$$σ = \frac{nαc}{4π} \qquad (3)$$

where c is the speed of light and $α$ is the absorption coefficient. The variation of the optical conductivity ($σ$) with photon energy ($hυ$) is shown in Fig. 2b. The optical conductivity increases gradually with a peak around the photon energy (3.45 eV) corresponding to the excitonic peak of the ZnO NCs. The two important energy loss functions [(i) volume energy loss function (VELF), (ii) surface energy loss function (SELF)] are studied to assess the rate of energy loss inside ZnO nanomaterial under electron transport. The VELF and SELF identified with the real and imaginary components of the dielectric constant as follows[45]:
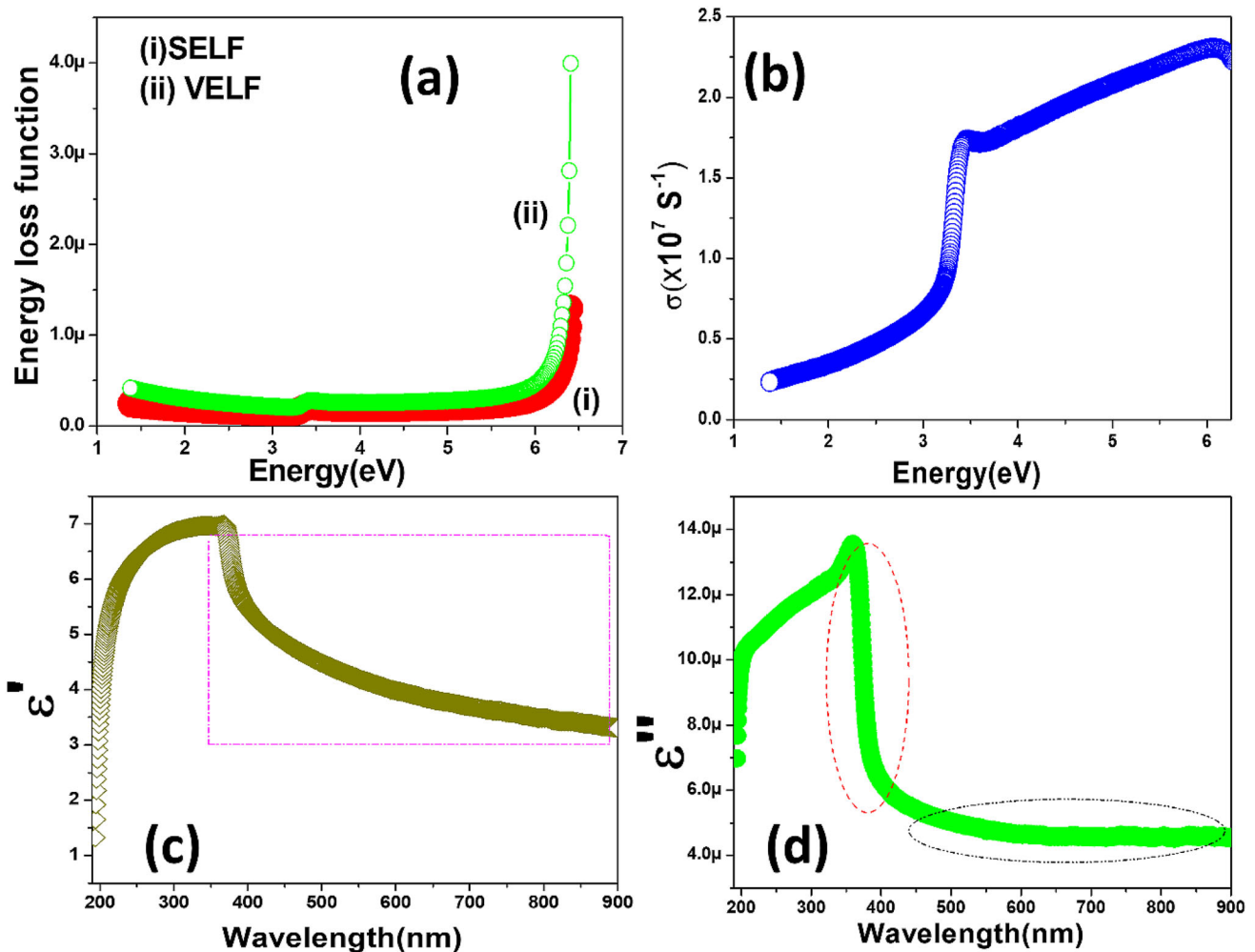
Fig. 2 **a** Plot of Energy loss functions with photon energy (*hυ*) of ZnO NCs; **b** plot of optical conductivity (*σ*) vs. *hυ*; **c** plot of real part of dielectric constant vs. wavelength; **d** variation of imaginary part of dielectric constant vs. wavelength

$$\text{Volume energy loss (VELF)} = \frac{\varepsilon''}{((\varepsilon')^2 + (\varepsilon'')^2)} \quad (4)$$

$$\text{Surface energy loss (SELF)} = \frac{\varepsilon''}{\left\{((\varepsilon' + 1)^2 + (\varepsilon'')^2)\right\}} \quad (5)$$

The graphical plot of VELF from Eq. (4) and SELF from Eq. (5) with the photon energy ($\varepsilon = h\upsilon$, unit eV) appeared in Fig. 2a. It is likewise certain that there is no huge contrast among SELF and VELF, especially at higher photon energies (up to 3.25 eV), yet the VELF expands more than SELF beyond the photon energy 3.5 eV. Above $\varepsilon = 5$ eV, increase of VELF is much faster than SELF with a significant difference. The real and imaginary components of the optical dielectric functions (ε', ε'') are in like manner concentrated by optical

spectroscopy, which are helpful in the affirmation of the general band structure of the nanomaterial. The optical refractive index (*n*) and dielectric constants are two useful parameters used for portraying the optical properties of semiconductor ZnO nanomaterial [66]. The calculated value of *n* and *K* are used to calculate the optical dielectric parameters (ε', ε'') utilizing the accompanying relations (6) and (7) [46]:

$$\text{Real part of the optical dielectric constant } (\varepsilon') = n^2 - K^2 \quad (6)$$

$$\text{Imaginary part of the optical dielectric constant } (\varepsilon'') = nK \quad (7)$$

Figure 2c and d show the graphical variations of ε' and ε'' with wavelength, respectively, for ZnO NCs.

The ε' value increases sharply up to $\lambda \approx 372$ nm with maximum value ≈ 7, then gradually decreases (marked by a pink-dotted rectangle in Fig. 2c). It tends to be seen that at higher wavelengths ($\lambda > 460$ nm) the optical dielectric (both ε' and ε'') constants are steady. The real part of the optical dielectric constant shows the amount it will hinder the speed of light in the material and is related to the refractive record ($n \approx \sqrt{\varepsilon'}$). The variation of ε'' of the ZnO NCs with wavelength ($\lambda = hc/\varepsilon$) is shown in Fig. 2d. The ε'' value is an almost constant form $\lambda \approx 460$ nm (marked by black dotted oval), but ε' slowly decreases in nature beyond this wavelength and almost constant above $\lambda \approx 700$ nm. The ε'' value increases up to $\lambda \approx 360$ nm with a small peak around 206 nm ($\varepsilon'' = 0.00000103$). The maximum value of ε'' (0.0000135) arises at $\lambda \approx 360$ nm or $\varepsilon \approx 3.44$ eV. Above 360 nm it falls sharply in almost constant average value of wavelength (374 nm) just similar like a Dirac delta function (marked by red dotted oval). It decreases very slowly from $\lambda \approx 405$ nm to 460 nm and constant change arises beyond $\lambda \approx 460$ nm. The imaginary part (ε'') of the optical dielectric constant identifies to the absorption coefficient [47]. It was represented that the ε'' dominatingly depicts the electron transition between the occupied and unoccupied states. The process of transition of electrons between the bands of a solid is notable by interbond absorption process. The absorption edge is achieved by the beginning of optical changes over the fundamental band gap of a semiconductor material.

3.2 Photoluminescence spectrum

The room temperature photoluminescence spectrum of the fabricated ZnO NCs with excitation wavelength (λ_{ext}) 345 nm is shown in Fig. 3. The photoluminescence spectrum or emission spectrum contains two peaks, one at $\lambda \approx 385.5$ nm and another at $\lambda \approx 574$ nm. The observed two peaks (385.5 nm and 574 nm) are fitted by multiple Gaussian curve fitting (see Supplementary materials Fig. S2). The area (A) of the Gaussian curves at 385.5 nm and 574 nm are $A_1 \approx 6.51$ Sq. unit and $A_2 \approx 36.28$ Sq. unit, respectively (see Table 1 for exact values). The UV long wavelength (UV A) emission at $\lambda \approx 385.5$ nm shows a full width at half maximum (FWHM) of around 28 nm. This peak may be ascribed to the radiative annihilation of excitons [14, 48]. This UV emission is also due to the high-purity and ideal
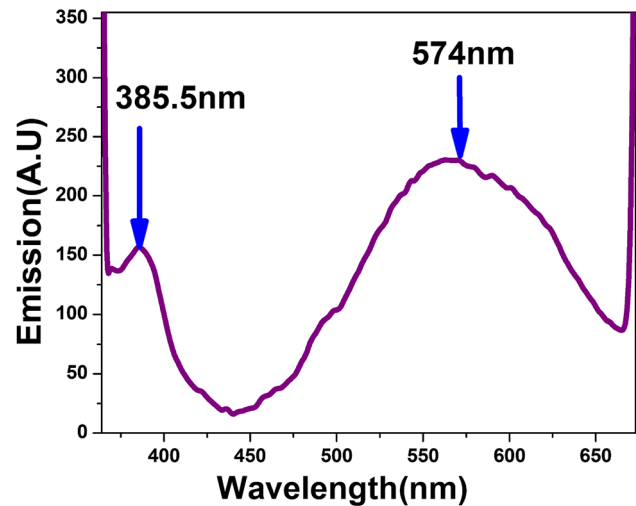
**Fig. 3** Photoluminescence spectrum of as-prepared ZnO NCs at room temperature

crystal structure of the grown ZnO NCs [48]. The edge of the yellow-green band emission at $\lambda \approx 574$ nm arises may be due to single ionized O-vacancy in ZnO NCs and came about because of the recombination of a photogenerated hole with a single ionized charge condition within the imperfections.

The strong yellow-green edge emission additionally implied that there were few surface imperfections (or defects) inside the ZnO nanocrystals [49]. The surface imperfections might be because of the chemical synthesis of the ZnO nanocrystals. The observed strong UVA emission is almost near band edge emission for the wide band gap energy (3.72 eV) ZnO NCs, due to the quantum confinement effect in the nanoregion. Quantum yield was resolved from the area of the multiple Gaussian fitting at two different emission maxima [50]. The quantum yield of the yellow-green light edge emission peaks was larger than UVA wavelength emission regions. Distinctive photoluminescence optical parameters are tabulated in Table 1.

3.3 Transmission electron microscopy (TEM) images

Figures 4d, 5, and S3(d) (see Supplementary Fig. S3) contain the TEM image of the fabricated ZnO nanocrystals. We compare the shape/morphology of the fabricated ZnO NCs with the buds on the twig of the Jasminum flower. Photographs of the flower 'twig Jasminum flowers' (Fig. S3 (a), (b), (c)) were taken from a nearby garden. The morphology of the

Fig. 4 a and **c** TEM micrograph of the as-prepared ZnO NCs; **b** a bud-shaped nanocrystal zooms from the marked portion of **a**
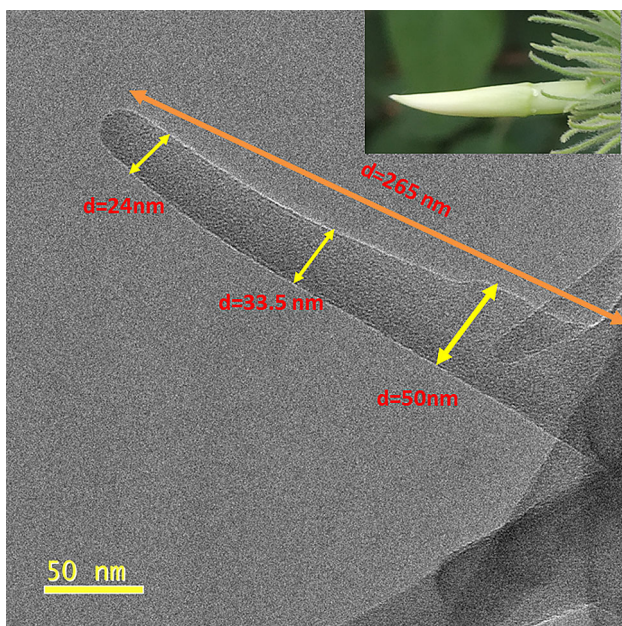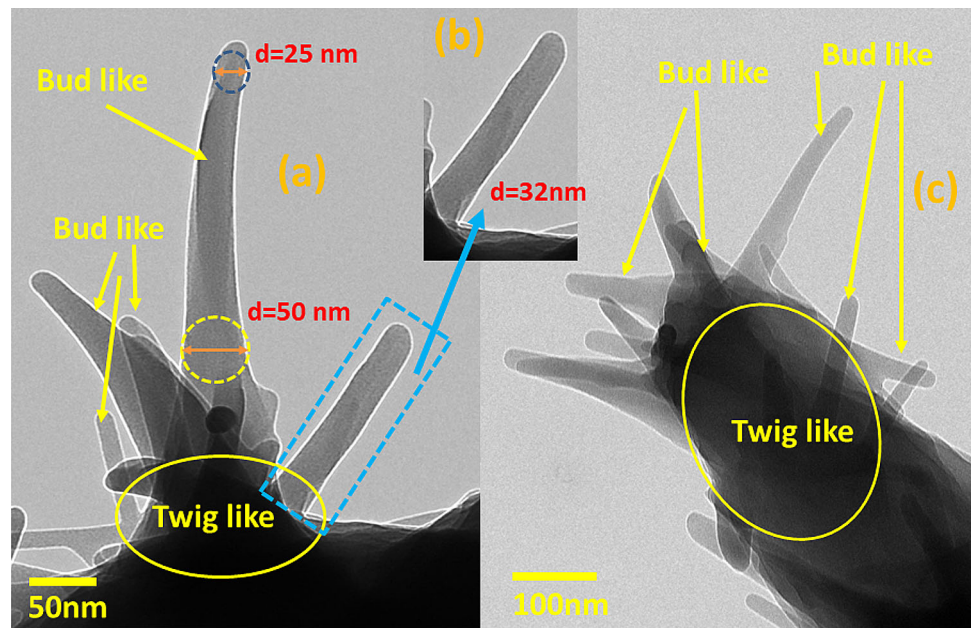
Fig. 5 TEM micrograph of a single ZnO nanobud; inset is the single bud of the Jasminum flower

fabricated ZnO nanocrystals as observed from the TEM images are similar as the buds on the twig of the Jasminum flower photograph. Hence, the ZnO NCs can be considered as ZnO nanobuds. ZnO nanobuds with different lengths and diameters are formed on a twig of ZnO crystal. The twig with ZnO nanobuds shown in Fig. 4a contains different lengths and diameters of nanobuds, one nanobud marked by color has a lower portion diameter 50 nm and upper

portion diameter 25 nm in average diameter $\approx$ 35 nm. The bud-shaped nanocrystal zooms from the marked portion of Fig. 4a shown in Fig. 4b that have uniform diameter of 35 nm and it looks like a single nanorod. The twig type shown in Fig. 4c contains an almost uniform large number of bud-shaped ZnO nanocrystal with an average diameter $\approx$ 32 nm. A single isolated ZnO nanobud is shown in Fig. 5 with lower diameter 50 nm, middle diameter 35.5 nm, and upper portion diameter 24 nm. The average diameter and length of the ZnO nanobud are 36 nm and 265 nm, respectively. This single ZnO nanobud with average aspect ratio 7.36 is similar in shape/morphology to a flower's single bud shown in the inset of Fig. 5. The clear lattice fringes and FFT of the lattice images are shown in Fig. 6a and c, respectively. The lattice constant (*c*) is found to be 0.52 nm as marked by red parallel fringe lines on the image (Fig. 6a). Figure 6b shows the corresponding SAED pattern of the ZnO NCs. The SAED pattern shows the well crystalline nature of the ZnO NCs with bright spots and diffraction planes corresponding to the hexagonal crystal phase. The lattice constant from fringe pattern and indexed SAED patterns are well supported with the XRD results.

3.4 X-ray powder diffraction (XRD) study

The XRD pattern of the fabricated power semiconductor ZnO NCs sample is shown in Fig. 7a. The

Fig. 6 **a** High-resolution electron micrograph of the ZnO NC. The imaged lattice spacing amounts to 0.52 nm; **b** corresponding SAED pattern; **c** image of the corresponding (fast Fourier transform) FFT of the image
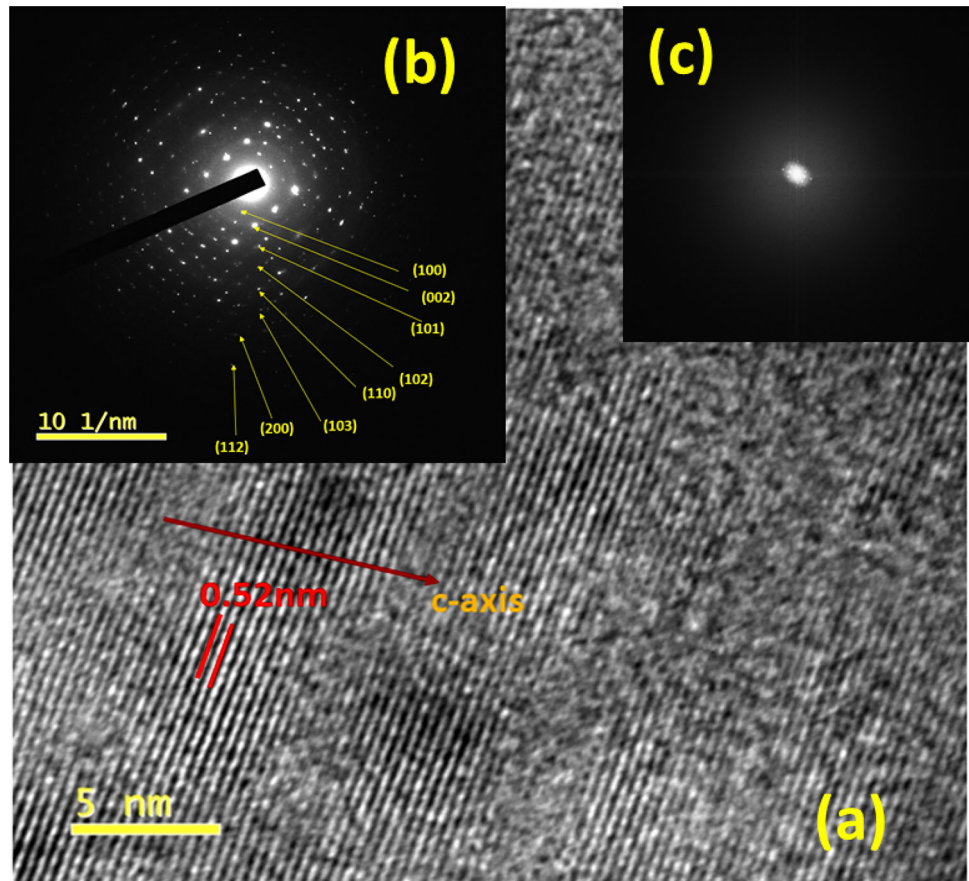
power diffraction pattern shows the following diffraction peaks: (100), (002), (101), (102) (110), (103), (200), (112), (201), (004), and (202) within the diffraction angle (2θ) 20° to 80°. The above diffraction peaks correspond to the index of the hexagonal crystal structure [51]. The lattice constants of the ZnO NCs with hexagonal lattice structure are calculated and found to be a = 3.2375 Å *and* c = 5.1945 Å. The average crystallite size (D_{hkl}) is determined from the accompanying Scherrer formula (SF) (Eq. (8)) [52, 53]:

$$D_{hkl} = \frac{k\lambda}{\beta \cos\theta} \qquad (8)$$

where λ = X-ray wavelength, β = width of the diffraction peak, generally measured as FWHM after instrumental broadening correction. The Scherrer constant (k) ranges from 0.62 to 2.08 [54]. In this study, k = 0.89 was used. The calculated ZnO NC size from Eq. (8) (considering the Gaussian nature of each diffraction peak) corresponding to different diffraction planes are shown by histogram diagram in Fig. 7b. Histogram of full width at half maxima (FWHM = β or $\beta_{1/2}$) with different diffraction peaks

is shown in Fig. 8b. The strain (ε) and dislocation density (δ) of the grown ZnO NCs is determined by applying the accompanying recipes: [55]:

$$\varepsilon = \frac{\beta}{4\tan\theta}, \quad \delta = \frac{1}{(D_{hkl})^2}$$

The strain (ε) and grain size (D) of the ZnO NCs is additionally determined utilizing Eq. (9), called Williamson–Hall equation (W–H) [56] (Tables 2 and 3):

$$\beta \cos\theta = \frac{k\lambda}{D} + 4\varepsilon \sin\theta \qquad (9)$$

The W–H plot comparing to ZnO NCs is shown in Fig. 8a. The Average ZnO NCs size from S–F equation (Eq. (8)) and W–H plot is found to be ≈ 28 nm and ≈ 36 nm, respectively. The determined estimation of strain is 0.0030 and 0.0015 from the SF and the fitted consequence of the W–H condition separately (see Table 4). The average dislocation densities are 1.28×10^{-3}/nm^2 and 7.72×10^{-4}/nm^2 from SF and W-H individually. The volume of the unit cell (V) and atomic fraction (A_f) are calculated from the accompanying formulas [39, 57]:

Fig. 7 **a** The XRD pattern of the ZnO NCs, **b** histogram of the variation of nanoparticles size corresponding to different diffraction planes
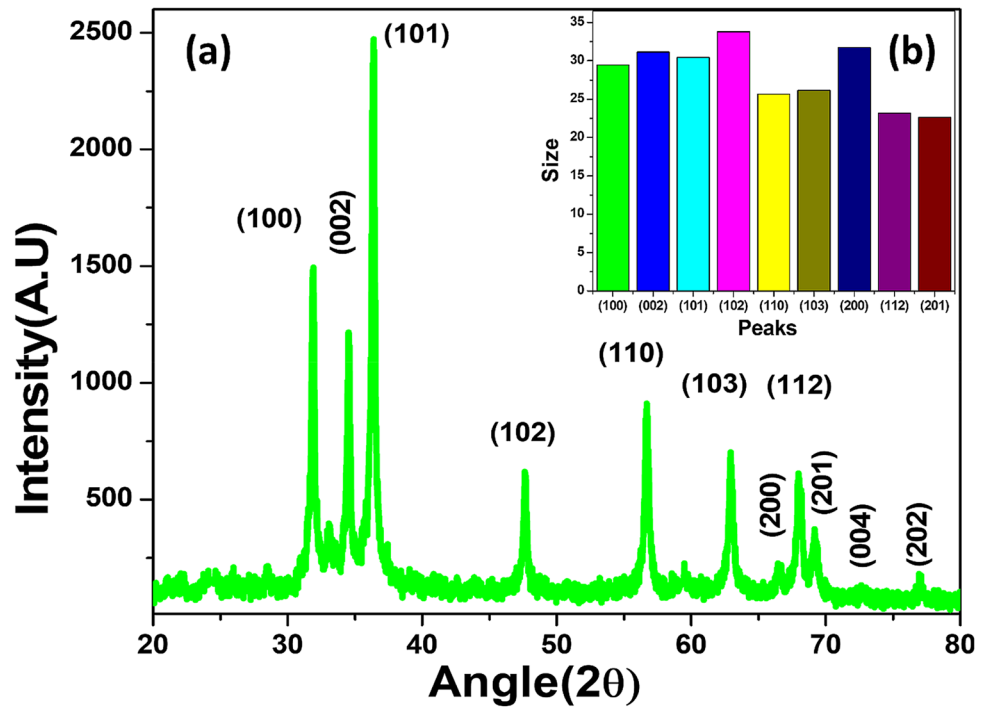
Fig. 8 **a** Variation of the $\beta_{1/2}\cos\theta$ vs. $4\sin\theta$ with fitted straight line, **b** histogram of $\beta_{1/2}$ with different diffraction peaks
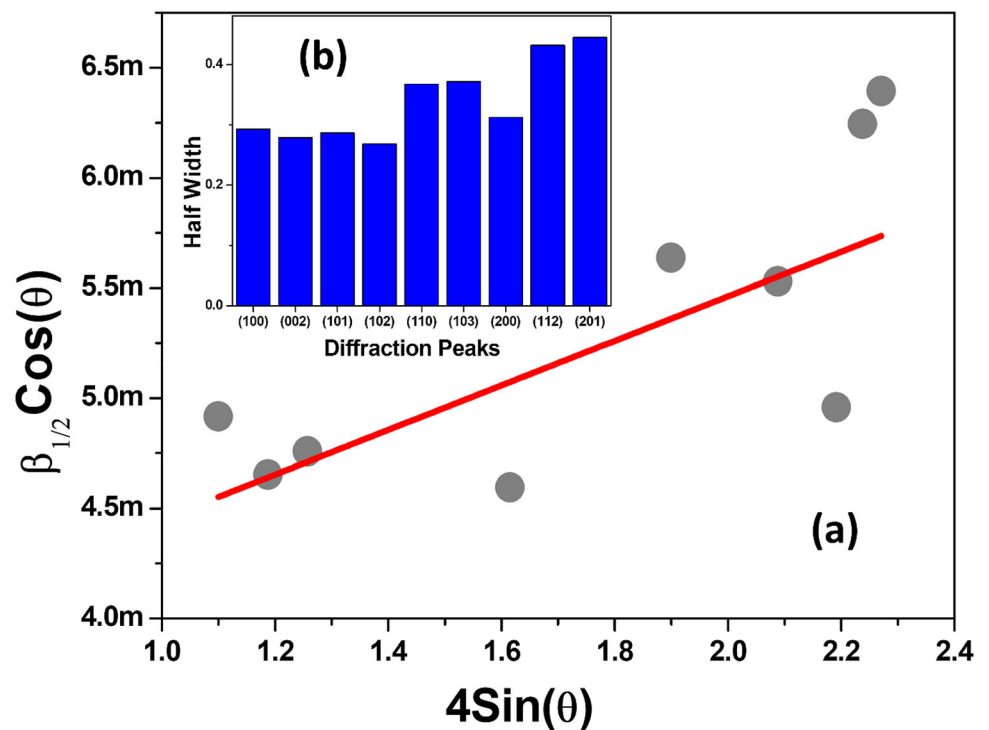
$$R_{hkl} = \frac{0.89\lambda}{\beta\cos\theta}, \quad V = \frac{\sqrt{3}}{2}a^2c, \quad A_f = \frac{2\pi a}{3\sqrt{3}c}$$

The value of V and A_f is found to be 47.1485 and 74.369%, respectively. The X-ray powder diffraction design shows that the development of the ZnO

nanocrystals during the chemical grown process is anisotropic and the growth rate along various directions is non-uniform.

To comprehend the anisotropic growth, let us compute the texture coefficient $T(h_ik_il_i)$ relating to the diffraction planes with Miller indices (hkl).

Table 2 Calculated texture coefficient of different ZnO nanostructures

Sample	Morphology	Average size from W–H	Average size from SF	Average size (nm)	Plane	Texture coefficient (T)
ZnO NCs	Budding twigs of flower	≈ 36	≈ 28 nm	32 nm	(100)	0.7067
					(002)	0.7525
					(101)	0.6717
					(102)	0.7282
					(110)	0.7715
					(103)	0.6986
					(200)	1.4701
					(112)	0.6824
					(201)	0.9836
					(004)	2.1148
					(202)	1.4458

Table 3 Size and lattice parameters

Sample	Morphology	Strain	Residual stress (σ)	Lattice constants		Unit cell volume	Atomic fraction (%)
				a (Å)	c (Å)		
ZnO NCs	Budding twig of flower	0.0020	− 0.5415	3.2375	5.1945	47.1485	74.3695

Table 4 Strain from half width and W–H equation

Sample	Strain (ε), $\varepsilon = \frac{\beta_{1/2}}{4\tan\theta}$	Strain (ε from W–H plot	Average (ε)
ZnO NCs	0.0030	0.0015	0.0020

The texture coefficient is determined from the following relation (Eq. (10)) [58]:

$$T(h_ik_il_i) = \frac{I(h_ik_il_i)}{I_0(h_ik_il_i)}\left[\frac{1}{n}\sum_{i=1}^{n}\frac{I(h_ik_il_i)}{I_0(h_ik_il_i)}\right]^{-1} \quad (10)$$

Here, $I(h_ik_il_i)$ and $I_0(h_ik_il_i)$ are the intensities of the specific (hkl) crystal plane of the ZnO NCs and that from the standard incentive from JCPDS consequence of the ZnO tests. The maximum and minimum values of T obtained from Eq. (10) are 2.1148 and 0.6717, respectively. The outcomes from the XRD investigation are summed up in Table 2. The experimental findings are in well concurrence with that from the standard JCPDS information.

3.5 Electrical properties of the as-synthesized ZnO nanorods

### 3.5.1 Current–voltage (I–V) characteristics

The current (I)–voltage (V) characteristics of the nano-ZnO/p-Si heterojunction diode were measured at room temperature in the dark and under UV irradiation of wavelength (i) ≈ 366 nm with incident optical power ≈ 100 mW. The I–V characteristics under dark and UV irradiation are shown in Fig. 9a and b, respectively. In the I–V variation, there are two regions (I and II). Region I is from 0 to 0.6 V and region II is from 0.6 V to 1.5 V. Here, 0.6 V is considered a turn-on voltage of the heterojunction. The interface of the regions is marked by the dotted line at V = 0.6 V. The nonlinear characteristics of the I–V behaviors of the fabricated heterojunction device can be expressed by the following equation (Eq. (11)) [59, 71]:

$$I = I_0\left[\exp\left(\frac{qV}{\eta k_BT}\right) - 1\right] \quad (11)$$

where T = temperature and k_B = Boltzmann constant.

It is obvious from the I–V characteristics (Fig. 10) that the nano-ZnO/p-Si heterojunction possesses

Fig. 9 Current (*I*)–voltage (*V*) characteristics for nano-ZnO/p-Si homojunction: **a** in the dark and **b** under UV light. The inset is the ln (*I*) vs. *V* plot (*V* > 0 volt): **a** in the dark and **b** under UV light
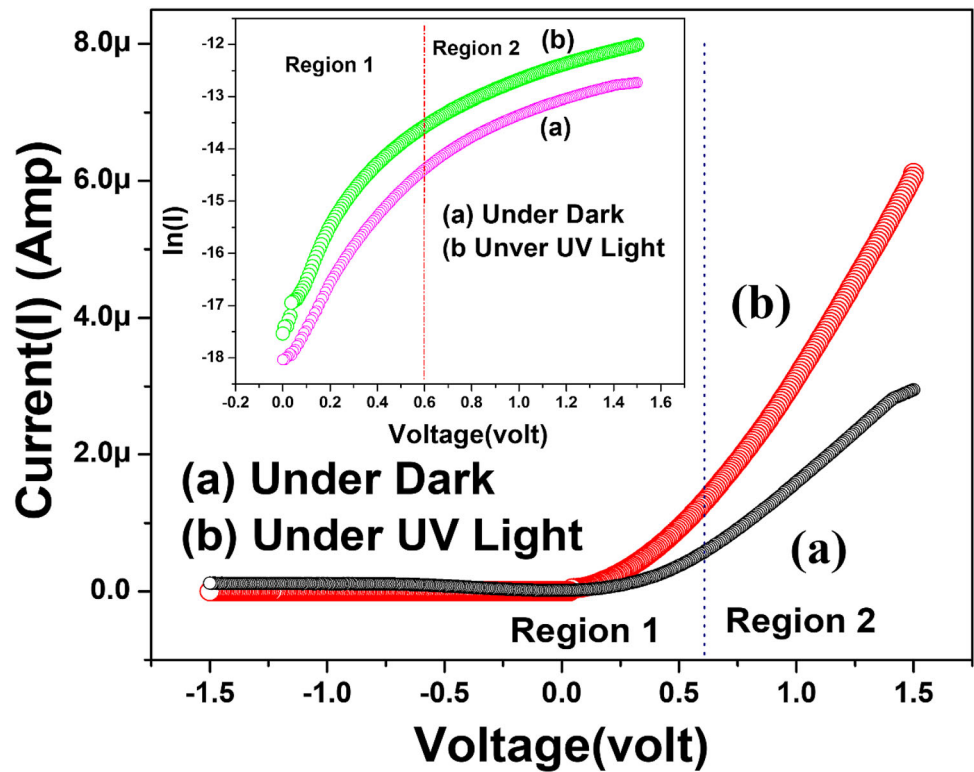
good rectification with a forward to reverse current proportion (I_F/I_R) of 5.63 at voltage 0.6 V and 46.2 at voltage 1.2 V under dark conditions, which increment to 46.2 and 219.3 under long wavelength (366 nm) UV light illumination at voltage 0.6 V and 1.2 V, respectively.

The ideality factor (η) and reverse saturation current (I_0) are calculated from ln (*I*) vs. *V* plot (see inset of Fig. 9). In the voltage region 0 to 0.6 V, the saturation current (I_0) and diode ideality factor (η) under dark conditions are 1.65×10^{-8} Amp and 6.25, respectively. In the voltage region 0.6 to 1.5 V, the value of η under dark is 2.5. Under the UV light exposed condition, in the voltage region 0 to 0.6 V, the value of I_0 and η are 1.1×10^{-7} Amp and 5.5, respectively. The higher voltage range, i.e., 0 to 1.5 volt under light shows ideality factor $\approx$ 2. The large value of ideality factor (2 to 6) in this experimental outcome of the heterojunction diode is due to lattice mismatch and edge dislocation of the junction, the development of the strain in the fabricated thin film [60], and the formation of grain boundaries at the nano-ZnO/Si interface [61]. The calculated values of η under dark and under UV light exposed condition of the fabricated Si/ZnO heterojunction are quite large, demonstrating the heterojunction to be far from

an ideal *p–n* junction. Along these lines, the ideal model can't clarify the current transport mechanism through the heterojunction. It appears that there are multiple transport mechanisms such as defect-assisted tunneling and transporter recombination in the space charge region by means of interface states [62]. The large value of the ideality factor of heterojunction device is also reported by different researchers [63]. The results reported by Tansely et al. showed high ideality factor close to 5 for n–n and 7 for p–n junction [64]. In their report, saturation current I_0 falls in the range 9×10^{-9} to 2×10^{-7} Amp with cut-in voltage 0.5 V.

The photoresponsivity (*R*) and external photodetection efficiency of the diode are expressed by the following expressions [65]:

$$R = \frac{I_{ph}}{P_{out}} \quad \text{and} \eta_{ext} = \left(\frac{hc}{q\lambda}\right) R \approx 1240 \left(\frac{R}{\lambda}\right)$$

where P_{out} is the incident optical power, I_{ph} = output photocurrent, and λ = Wavelength of the incident light. The calculated *R* and η_{ext} at the voltage 0.6 V are 0.015 and 5.5%, respectively. The values of *R* and η_{ext} at the voltage 1.5 V are 0.065 and 21.5%, respectively. Hence the fabricated heterojunction device exhibits good UV-photoresponse properties.
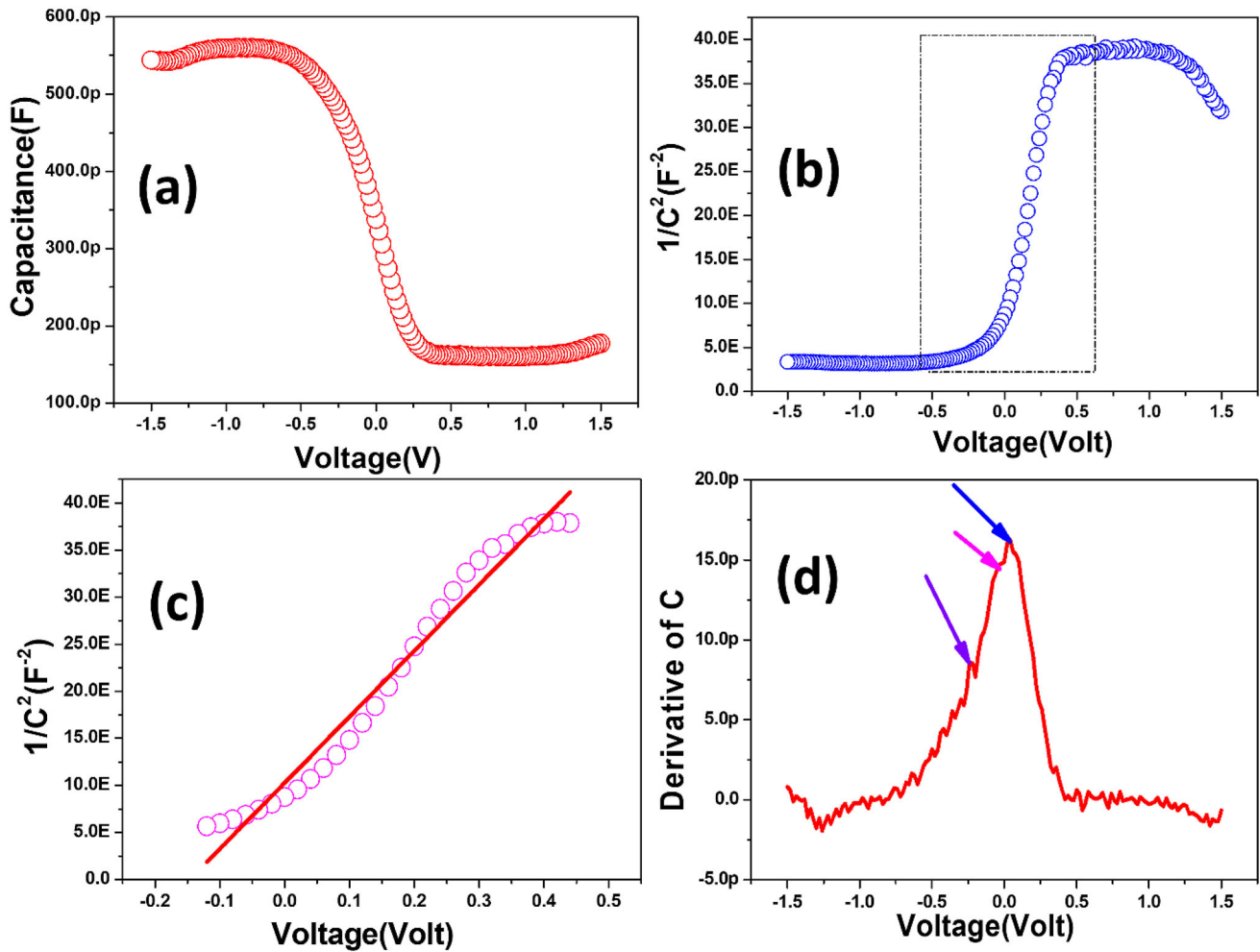
Fig. 10 **a** Capacitor (*C*)–voltage (*V*) characteristics for nano-ZnO/p-Si homojunction under Dark condition, **b** plot of $1/C^2$ vs. voltage (*V*) with full measured voltage range, **c** plot of $1/C^2$ vs. voltage (*V*) of the linear region and corresponding fitted straight line, **d** plot of derivative of *C* vs. *V*
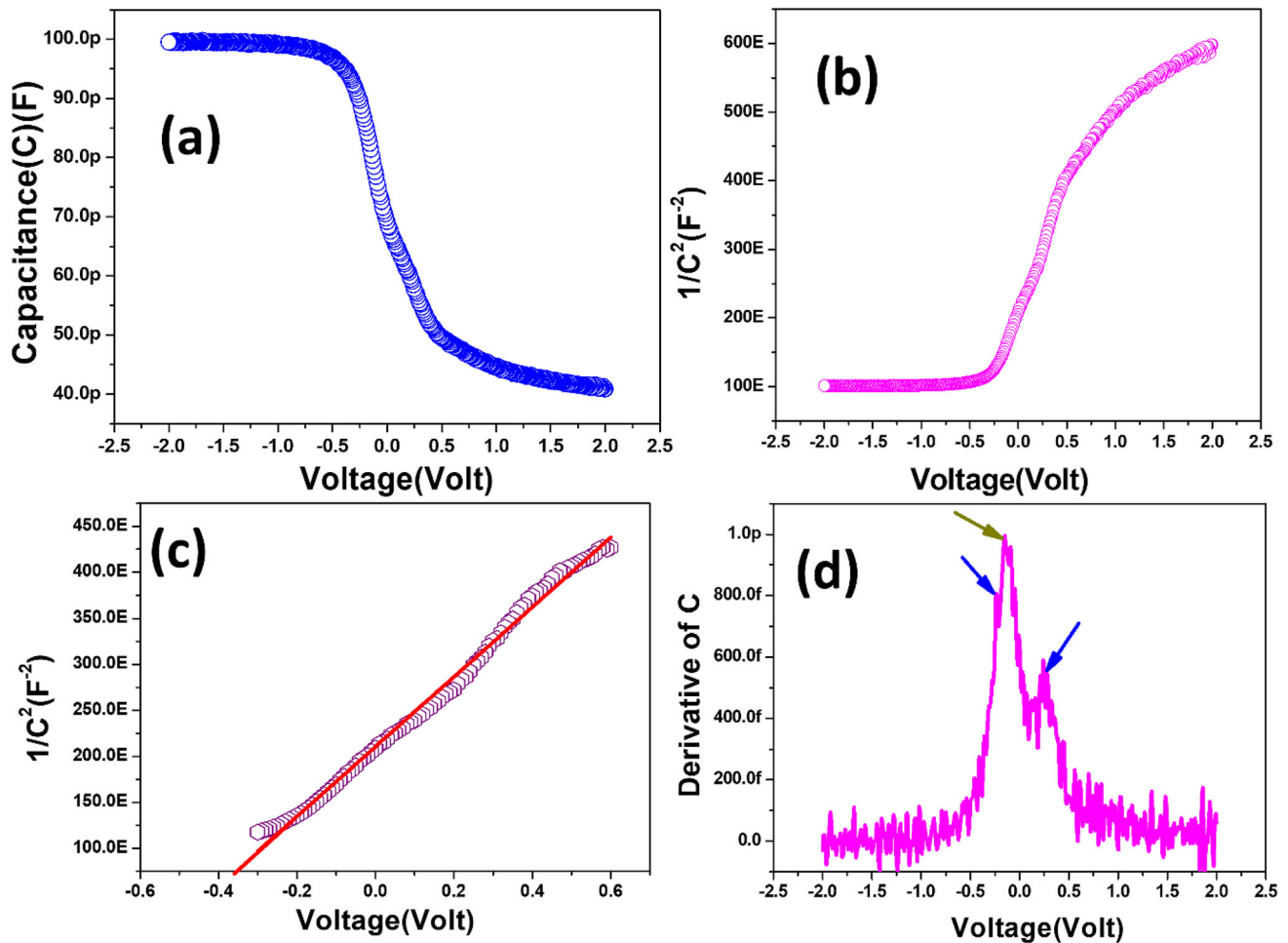
3.5.2 Capacitor (C)–voltage (V) characteristics

The capacitor (*C*)–voltage (*V*) characteristics of the heterojunction is measured under the high frequency of 500 kHz. The *C*–*V* characteristics are studied under dark and under the presence of UV light shown in Fig. 10a and 11a, respectively. The nature of *C*–*V* plots is equivalent to the nature of the *C*–*V* curve represented by Majumder et al. [60]. The connection between the capacitance per unit area and the voltage in the customary heterojunction theory can be expressed as Eq. (12) [67]

$$\frac{1}{C^2} = \frac{2(V_{bi} - V)}{q\varepsilon_s N_D} \tag{12}$$

Here, we consider $V \gg kT/q$ and $N_A \gg N_D$, where V_{bi}, *V*, ε_s, and N_D represent built-in potential, basing

voltage, permittivity of ZnO, and donor concentration, respectively. Figures 10b and 11b show $1/C^2$ versus *V* plot with full measured voltage range under dark and under the presence of UV light irradiation on the heterojunction, respectively. Figures 10c and 11c show plot of $1/C^2$ vs. voltage (*V*) of the linear region of the *C*–*V* graph under dark and under the UV light irradiation, respectively. Figures 10c and 11c show $1/C^2$ versus *V* plot where the linear region intercept along the x-pivot gives built-in potential and the slant can be utilized to infer the donor concentration utilizing the accompanying condition: $N_D = 2/(q\varepsilon_s \times \text{slope})$.

The calculated barrier height and donor concentration under dark and light conditions are shown in Table 5. The average value acquired for the built-in potential and donor concentration (N_D) was found to

Fig. 11 **a** Capacitor (*C*)–voltage (*V*) characteristics for nano-ZnO/p-Si homojunction under UV light irradiation condition, **b** plot of $1/C^2$ vs. voltage (*V*) with full measured voltage range, **c** plot of 1/ C^2 vs. voltage (*V*) of the linear region and corresponding fitted straight line, **d** plot of derivative of *C* vs. *V*

be 0.25 eV and 1.5×10^{17} cm^{-3} separately. The barrier height (ϕ_c) of the p–n heterojunction can likewise be assessed from C–V plot utilizing the accompanying condition (Eq. (13)) [63, 67]:

$$\phi_c = V_{bi} + \left(\frac{k_B T}{q}\right) \times \left[1 + \ln\left(\frac{N_C}{N_D}\right)\right] \qquad (13)$$

The value of capacitance decreases in the presence of light, but the barrier height increases slightly in the presence of light. This may be due to the rate of

increase in the accumulation of carriers which is less compared to the rate of increase of the development of the barriers potential about the junction with incident UV light. This implies the active participation of the electron traps in the depleted zone [66]. Figures 10d and 11d show the plot of derivative of *C* vs. *V* under dark and under the UV light irradiation on the heterojunction, respectively. The presence of few peaks in the derivative of the *C*–*V* graph suggests the presence of electron traps. The diffusion voltage

Table 5 Different characteristics parameters from *C*–*V* characteristics of the nano-ZnO/p-Si heterojunction UV light photodiode

Condition	Built-in potential (eV)	N_D (cm^{-3})	Barrier height (ϕ_c), eV	Depletion width (W_{Dep}), μm	Diffusion voltage (V_{do}), eV
Dark	0.15	2×10^{17}	0.25	0.320	0.176
UV light	0.35	1×10^{17}	0.477	0.447	0.376

Fig. 12 a Heterojunction band diagram of nano-ZnO/p-Si, b the schematic structure of nano-ZnO/p-Si heterojunction photodiode
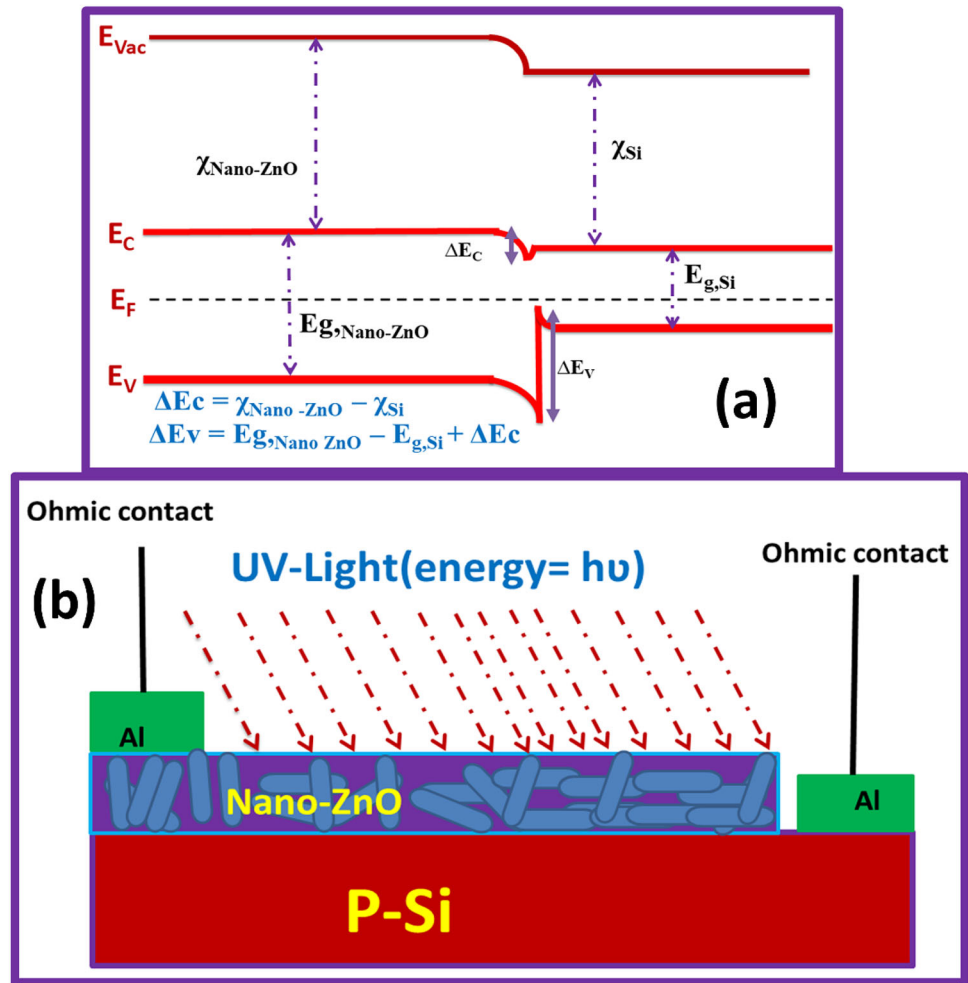
(V_{do}) of the junction can be calculated from the following equation (14) [67]:

$$V_{do} = v_{bi} + \frac{k_B T}{q} \qquad (14)$$

The resultant calculated values are tabulated in Table 5. The depletion width of the fabricated heterojunction diode can be obtained from the below Eq. (15) [68]:

$$W_{Dep} = \sqrt{\left[\frac{\varepsilon_0 \varepsilon_s (V_{bi} - V)}{q N_D}\right]} \qquad (15)$$

The average value obtained for depletion width was found to be 0.3835 μm.

3.5.3 Energy band diagram and carrier transport

The energy band diagram of the nano-ZnO/p-Si nano heterojunction diode is depicted in Fig. 12a. The Fermi energy level (E_F) of the fabricated heterojunction is drawn by considering n-type ZnO nanocrystals (Fig. 12a), as-grown ZnO is maximum time n type due to native defects [66]. The conduction band (E_c), valence band (E_v), and vacuum level (E_{vac}) are shown in the Fig. 12a. The band gap of p-Si $(E_{g,Si})$ is 1.12 eV [69], nano-ZnO is $(E_{g,Nano\ ZnO})$ 3.72 eV, and the electron affinity of ZnO $(\chi_{Nano\ ZnO})$ and p-Si (χ_{Si}) are 4.4 eV and 4.05 eV, respectively [60, 69]. The energy band diagram is drawn by considering type-II heterojunction [70]. The band diagram shows a small conduction band offset of 0.35 eV as calculated by $\Delta E_c = \chi_{Nano\ ZnO} - \chi_{Si}$ and a large valence band offset 2.95 eV calculated by $\Delta E_v = E_{g,Nano\ ZnO} - E_{g,Si} + \Delta E_c$ [70]. There is a diffusion of electrons from n-ZnO nano to p-Si and a diffusion of holes from p-Si to n-ZnO nano. At low, forward voltage, the current is limited by a space charge region; however, by increasing the forward voltage, the depletion width

decreases and current increases exponentially, following Eq. (11).

4 Conclusion

We have successfully investigated the structural and optical properties of chemical precipitation-derived budding twigs of Jasminum flower-like ZnO nanocrystals for the fabrication of UV-light-dependent heterojunction photodiode. A high-quality optical property of the pure ZnO NCs was suggested by photoluminescence and absorption spectroscopy. By measuring ultraviolet (UV) light-dependent ($\lambda \sim 366$ nm) and dark condition current (I)–voltage (V) as well as capacitance (C)–voltage (V) characteristics, the junction and photodetection properties of the fabricated nano-ZnO/p-Si heterojunction photodiode were successfully examined. The diode showed a well-defined rectifying behavior with a photoresponsivity and external photodetection efficiency of 0.065 and 21.5%, respectively. The heterojunction band diagram of nano-ZnO/n-Si is proposed, and an endeavor is made to decide the most prominent change in junction capacitance and the barrier height under UV irradiation with the knowledge of the current transport mechanism. The discussed characteristics indicate a successful fabrication of a low-cost and good rectifying nano-ZnO/p-Si heterojunction with UV-enhanced performance. The qualities of the device demonstrate that it tends to be used for UV photodetection applications in nano-optoelectronic and photonic devices. The UV irradiation-dependent performance of the diode likewise can be used in various applications where a wide band gap, semiconductor-based devices perform better. These discussions give an idea of the nanocrystalline ZnO semiconductor for good UV photodetection performance of low-cost nano-ZnO/n-Si heterojunction devices.

Authors' contributions

AKB assisted the problem of the research, carried out the measurement, and manuscript writing. SS assisted the measurement, discussed and helped in drafting the manuscript. All authors read and approved the final manuscript.

Data availability

The data that support the findings of this study are available within the article.

Declarations

Conflict of interest The authors declare that they have no conflict of interest.

Research involving humans and animals' statement This article does not contain any studies involving humans and animals performed by any of the authors.

Supplementary Information: The online version contains supplementary material available at https://doi.org/10.1007/s10854-021-05649-4.

References

1. A. Tsukazaki, A. Ohtomo, T. Onuma, M. Ohtani, T. Makino, M. Sumiya, K. Ohtani, S.F. Chichibu, S. Fuke, Y. Segawa, H. Ohno, H. Koinuma, M. Kawasaki, Nature Materials **4**, 42–46 (2005)
2. Ü. Özgür, Y.I. Alivov, C. Liu, A. Teke, M.A. Reshchikov, S. Doğan, V. Avrutin, S.-J. Cho, H. Morkoç, J. Appl. Phys. **98**, 041301 (2005)

3. D. Vanmaekelbergh, L.K. van Vugt, Nanoscale **3**, 2783–2800 (2011)

4. A.B. Djurišić, Y.H. Leung, Small **2**(8–9), 844–961 (2006)

5. V.S. Bhati, M. Hojamberdiev, M. Kumar, Energy Rep. **6**(4), 46–62 (2020)

6. H.M. Xiong, Y. Xu, Q.G. Ren, Y.Y. Xia, J. Am. Chem. Soc. **130**(24), 7522–7523 (2008)

7. R. Sinha, N. Roy, T.K. Mandal, A.C.S. Appl, Mater. Interfaces **12**, 33428–33438 (2020)

8. L. Zhang, L. Zhu, X. Li, Z. Xu, W. Wang, X. Bai, Sci. Rep. **7**, 45143 (2017)

9. A.B. Djurišic, A.M.C. Ng, X.Y. Chen, Progress Quant Electron **34**(4), 191–259 (2010)

10. M.H. Huang, S. Mao, H., Yan, H., Wu, Y., Kind, H., Weber, E., Russo, R. and Yang, P. , Room-temperature ultraviolet nanowire nanolasers. Science **292**(5523), 1897–9 (2001)

11. Nakamura, Y., 2006. Solution-growth of zinc oxide nanowires for dye-sensitized solar cells. Materials, Nnin Reu, Research Accomplishments, pp. 74–75

12. Y. Jin, J. Wang, B. Sun, J.C. Blakesley, N.C. Greenham, Nano Lett. **8**(6), 1649–1653 (2008)

13. Y.L. Chu, L.W. Ji, H.Y. Lu, S.J. Young, I.T. Tang, T.T. Chu, J.S. Guo, Y.T. Tsai, J. Electrochem. Soc. **167**, 027522 (2020)

14. L. Guo, Y.L. Ji, H. Xu, P. Simon, Z. Wu, J. Am. Chem. Soc. **124**, 14864–14865 (2002)

15. M.L. Pivert, R. Poupart, M.C. Gnambodoe, N. Martin, Y.L. Wang, Microsyst. Nanoeng. **5**, 57 (2019)

16. A.K. Bhunia, P.K. Samanta, S. Saha, T. Kamilya, Appl. Phys. Lett. **103**, 143701 (2013)

17. Y.W. Zhu, H.Z. Zhang, X.C. Sun, S.Q. Feng, J. Xu, Q. Zhao, B. Xiang, R.M. Wang, D.P. Yu, Appl. Phys. Lett. **83**, 144 (2003)

18. X. Xu, C. Xu, J. Hu, J. Appl. Phys. **116**, 103105 (2014)

19. D.I. Son, H.Y. Yang, T.W. Kim, W.I. Park, Compos. Part B Eng. **69**, 154–158 (2015)

20. Xi. Liu, G. Leilei, Q. Zhang, W. Jiyuan, Y. Long, Z. Fan, Nat. Commun. **5**, 4007 (2014)

21. K. Liu, M. Sakurai, M. Aono, Sensors **10**(9), 8604–8634 (2010)

22. P. Kumar, J. Liu, P. Ranjan, Y. Hu, S. Yamijala, S.K. Pati, J. Irudayaraj, G.J. Cheng, Small **1703346**, 1–10 (2018)

23. E. Matei, L. Ion, S. Antohe, R. Neumann, I. Enculescu, Nanotechnology **21**, 10 (2010)

24. P. Ranjan, P. Tiwary, A.K. Chakraborty, R. Mahapatra, A.D. Thakur, J. Mater. Sci. Mater. Electron. **29**, 15946–15956 (2018)

25. P. Ranjan, T.K. Sahu, R. Bhushan, S. Yamijala, D.J. Late, P. Kumar, A. Vinu, Adv. Mater. **31**, 1900353 (2019)

26. P. Ranjan, S. Agrawal, A. Sinha, T.R. Rao, J. Balakrishnan, A.D. Thakur, Sci. Rep. **8**, 1–13 (2018)

27. P. Ranjan, A. Tulika, R. Laha, J. Balakrishnan, J. Raman Spectrosc. **48**(4), 586–591 (2017)

28. P. Ranjan, P. Verma, S. Agrawal, T.R. Rao, S.K. Samanta, A.D. Thakur, Mat. Chem. Phys. **226**, 350–355 (2019)

29. H.D. Cho, A.S. Zakirov, S.U. Yuldashev, C.W. Ahn, Y.K. Yeo, T.W. Kang, Nanotechnology **23**, 115401 (2012)

30. S.K. Singh, P. Hazra, S. Tripathi, P. Chakrabarti, J. Mater. Sci. Mater. Electron. **26**, 7829–7836 (2015)

31. A.C. Saritha, M.R. Shijeesh, L.S. Vikas, R.R. Prabhu, M.K. Jayaraj, J. Phys. D Appl. Phys. **49**, 29 (2016)

32. A. Özmen, S. Aydogan, M. Yilmaz, Ceram. Int. **45**(12), 14794–14805 (2019)

33. R. Saha, A. Karmakar, S. Chattopadhya, Opt. Mater. **105**, 109928 (2020)

34. T.H. Flemban, M.A. Haque, I. Ajia, N. Alwadai, S. Mitra, T. Wu, I.S. Roqan, A.C.S. Appl, Mater. Interfaces **9**, 37120–37127 (2017)

35. L.J. Mandalapu, Z. Yang, S. Chu, J.L. Liu, Appl. Phys. Lett. **92**, 122101–122103 (2008)

36. J. Yu, N. Tian, Phys. Chem. Chem. Phys. **18**, 24129–24133 (2016)

37. M. Dutta, D. Basak, Appl. Phys. Lett. **2008**(92), 212112 (2008)

38. V. Kabra, L. Aamir, M.M. Malik, Beilstein J. Nanotechnol. **5**, 2216–2221 (2014)

39. A.K. Bhunia, T. Kamilya, S. Saha, Chem. Select **1**, 2872–2882 (2016)

40. A.K. Bhunia, S. Saha, BioNanoScience **10**, 89–105 (2020)

41. N.A. Al-Hamdani, R.D. Al-Alawy, S.J. Hassan, IOSR J. Comput. Eng. **16**, 11 (2014)

42. A.K. Bhunia, S. Saha, Adv. Sci. Eng. Med. **11**(7), 644–651 (2019)

43. L. Xu, G. Zheng, H. Wua, J. Wang, F. Gu, J. Su, F. Xian, Z. Liu, Opt. Mater. **35**, 1582 (2013)

44. J.I. Pankove, *Optical Processes in Semiconductors* (Courier Dover Publications, New York, 2012).

45. H.A. Mohamed, Optoelectron. Adv. Mater. **6**, 389 (2012)

46. T.N. Ghosh, A.K. Bhunia, S.S. Pradhan, S.K. Sarkar, J. Mater, Sci. Mater. Electron. **31**, 15919–15930 (2020)

47. S.B. Aziz, R.T. Abdulwahid, H.A. Rsaul, H.M. Ahmed, In situ synthesis of CuS nanoparticle with a distinguishable SPR peak in NIR region. J. Mater. Sci. **27**(5), 4163–4171 (2016)

48. A. Van Dijken, E.A. Meulenkamp, D. Vanmaekelbergh, A. Meijerink, J. Lumin. **87–89**, 454–456 (2000)

49. A.B. Djurišić, Y.H. Leung, K.H. Tam, L. Ding, W.K. Ge, H.Y. Chen, S. Gwo, Appl. Phys. Lett **88**, 103107 (2006)

50. A.K. Bhunia, S. Saha, Luminescence **36**(1), 149–62 (2021)

51. Z.R. Tian, J.A. Voigt, J. Liu, B. Mckenzie, M.J. Mcdermott, M.A. Rodriguez, H. Konishi, H. Xu, Complex and oriented ZnO nanostructures. Nat. Mater. **2**, 821–826 (2003)

52. A.K. Bhunia, P.K. Jha, S. Saha, BioNanoScience **10**, 917–927 (2020)

53. P. Scherrer, Bestimmung der Grösse und der inneren Struktur von Kolloidteilchen mittels Röntgenstrahlen. Nachr. Ges. Wiss. Göttingen **26**, 98 (1918)

54. J.I. Langford, A.J.C. Wilson, Scherrer after sixty years: a survey and some new results in the determination of crystallite size. J. Appl. Cryst. **11**, 102 (1978)

55. B.L. Chandrasekar, P. Raji, R. Chandramohan, R. Vijayalakshmi, G. Devi, P. Shunmugasundaram, P. Sindhu, J. Nanoelectron. Optoelectron. **8**(4), 369 (2013)

56. V.D. Mote, Y. Purushotham, B.N. Dole, WilliamsonHall analysis in estimation of lattice strain in nanometer-sized ZnO particles. J. Theor. Appl Phys. **6**(6), 1–8 (2012)

57. S.P. Mandal, K. Das, A. Dhar, S.K. Ray, Nanotechnology **18**, 095606 (2007)

58. V. Kumar, K. Singh, M. Jain, K.A. Manju, J. Sharma, A. Vij, A. Thakur, Role of Cu in engineering the optical properties of SnO_2 nanostructures: structural, morphological and spectroscopic studies. Appl. Surf. Sci. **444**, 552–558 (2018)

59. S.M. Sze, *Physics of Semiconductor Devices*, 2nd edn. (Wiley, New York, 1981).

60. S. Majumder, P. Baherji, J Appl Phys 105,043704 (2009)

61. F. Greutert, G. Blatter, Semicond. Sci. Technol. **5**, 111–137 (1990)

62. S. Mridha, D. Basak, Semicond. Sci. Technol. **21**, 928 (2006)

63. S. Aksoy, Y. Caglar, Superlattices Microstruct **51**, 613–625 (2012)

64. T.L. Tansley, J. Appl. Phys. **55**(2), 454 (1984)

65. G.M. Ali, P. Chakrabarti, IEEE Photon J. **2**, 784 (2010)

66. S. Mridha, D. Basak, J. Appl. Phys. **101**, 083102 (2007)

67. S. Chirakkara, S.B. Krupanidhi, Study of n-ZnO/p-Si (100) thin film heterojunctions by pulsed laser deposition without buffer layer. Thin Solid Films **520**(18), 5894–5899 (2012)

68. S.K. Nandi, S. Chatterjee, S.K. Samanta, P.K. Bose, C.K. Maiti, Bull. Mater. Sci. **26**, 693 (2003)

69. S. Adachi, *Hand Book on Physical Properties of Semiconductors II–VI Compound Semiconductors*, vol. 3 (Springer, New York, 2004).

70. F.B. Kevin, *The Physics of Semiconductors with Application to Optoelectronics Devices* (Cambridge University Press, Cambridge, 1999).

71. S. Mridha, M. Dutta, D. Basak, J. Mater. Sci. Mater. Electron. **20**, 376–379 (2009)